SAND2015-3156J

# An important criterion for reliable MMI diagnostics and its impact on the reconstructed images

T. Nagayama,[1, a)] R. C. Mancini,[1] D. Mayes,[1] R. Tommasini,[2] and R. Florido[3]
[1)] *Physics Department, University of Nevada, Reno, NV*
[2)] *Lawrence Livermore National Laboratory, Livermore, CA*
[3)] *Departamento de Física, Universidad de Las Palmas de Gran Canaria, 35017 Las Palmas de Gran Canaria, Spain*

(Dated: 27 March 2015)

Temperature and density asymmetry diagnosis is critical to advance inertial confinement fusion (ICF) science. A multi-monochromatic x-ray imager, MMI, records the spectral signature from an ICF implosion core with time resolution, 2-D spatial resolution, and spectral resolution. While narrow-band images and 2-D space-resolved spectra from the MMI data constrain temperature and density spatial structure of the core, the accuracy of the images and spectra highly depend on the quality of the MMI data and the processing tools. Here, we synthetically investigate the criterion for reliable MMI diagnostics and its effects on the accuracy of reconstructed images. The pinhole array tilt determines the object spatial sampling efficiency and the minimum reconstruction width, $w$. When the spectral width associated with $w$ is significantly narrower than the spectral line width, the line images reconstructed from the MMI data become reliable. The MMI setup has to be optimized for every application to meet this criterion for reliable MMI diagnostics.

## I. INTRODUCTION

Inertial confinement fusion (ICF) is a concept for an alternative energy source, which releases energy by compressing a millimeter-scale capsule containing fusion-fuel (i.e., hydrogen isotopes such as tritium, T, and deuterium, D) with ablation pressure driven by high power lasers[1,2]. Substantial progress has been made in theory, experiment, and diagnostics of ICF, but efficient fuel burn, *ignition*, has not yet been achieved due to discrepancies between experiments and simulations[3]. While sources of discrepancies are extensively investigated and many of them are being recognized[4], diagnostics that directly observe the evolution of the ICF implosion plasma spatial structure are desired to advance ICF science towards ignition.

Multi-monochromatic x-ray imagers (MMI) are attractive instruments for this purpose. MMI is a unique 2-D spectrometer consisting of a pinhole-array (PA), a multi-layered mirror (MLM), and a microchannel plate (MCP)[5,6]. It records an array of ICF implosion core images, each of which is formed by photons of slightly different wavelength. By processing MMI data, one can extract narrow-band images (i.e., intensity images of narrow spectral ranges), space-integrated spectra[7–9], and 2-D space-resolved spectra[10]. Spectroscopic analysis of the images and spectra extracted from the MMI data can provide a variety of approaches to constrain ICF plasma spatial structure in electron temperature, $T_e$, and electron density, $n_e$.

For example, we adde a small amount of Ar into $D_2$ fuel as a tracer and analyzed Ar line emission to characterize $T_e$ and $n_e$ of the core. Previously, we extracted time-resolved 2-D $T_e$ maps from two narrow-band images[11]. From a collection of space-resolved spectra, we extracted time-resolved 2-D $T_e$ and $n_e$ maps[10]. Synthetic investigations also suggest that time-resolved 3-D $T_e$ and $n_e$ spatial distributions of ICF cores can be extracted by simultaneously analyzing collections of 2-D space-resolved spectra extracted from three MMI instruments fielded along quasi-orthogonal lines of sight[12]. Thus, MMI diagnostics has potential to better constrain ICF experiments and advance ICF theory.

While MMI data are rich in information, MMI data with good signal do not necessarily provide reliable information. For reliable MMI diagnostics, it is important to efficiently sample an object's spatial information. This requires the MMI setup to be optimized for every application.

In this article, we discuss a criterion for reliable MMI diagnostics and show how this criterion affects the reliability of the extracted spatial information by reconstructing narrow-band images from synthetic MMI data. It is difficult to experimentally study the fidelity of the reconstructed images because what is expected of the image is not known a priori. These questions can be best addressed synthetically since the expected images can be computed. We show that the pinhole array tilt must be optimized to efficiently sample object spatial information and determine the minimum spectral width, $w$, of the image reconstruction. This reconstruction width has to be significantly narrower than the full-width at half-maximum (FWHM) of the diagnostic lines.

This article is organized as follows. Sec. II shows MMI data obtained with appropriate and inappropriate pinhole array designs and defines the criterion for reliable MMI diagnostics. Sec. III discusses the spectral model, which is used to create synthetic MMI data and also to compute expected images. In Sec. IV, the impact of the

[a)] Present address: Sandia National Laboratories, Albuquerque, NM

criterion is synthetically investigated using these models. The conclusions are given in Sec. V.

## II. PINHOLE ARRAY DESIGN AND IMAGE RECONSTRUCTION

MMI consists of a hexagonally allocated pinhole array (PHA), a multi-layered mirror (MLM), and microchannel plates (MCP), which provide 2-D spatial resolution ($\Delta x \approx 11\,\mu$m), spectral resolution ($E/\Delta E \approx 150$), and time-resolution ($\Delta t \approx 100$ ps), respectively. The given resolutions are typical values for our applications[10–12]. The spatial resolution depends on pinhole size and object-PHA-detector distances. Spectral and temporal resolution is determined by the specifications of the MLM and MCP, respectively. A key component for successful MMI data measurement is the PHA design, and it has to be optimized for every application. Here, we discuss necessary considerations to optimize the PHA design through the application to Ar doped ICF experiments.

Pinhole size is determined based on the expected signal levels on the detector and desired spatial resolution. Expected signal level on the detector depends on the object radiation power, the pinhole size, the object-PHA-detector distances, and the detector sensitivity. For example, when the ICF implosion core is diagnosed with signals from Ar tracer, the core radiation power needs to be estimated with a spectral model at $T_e$ and $n_e$ predicted from the hydrodynamic simulations. If the estimated signals seem too low for a given configuration, one can increase the signals on the detector by increasing the object radiation power, increasing the object solid angle to the pinhole, or improving the detector sensitivity. In our application, we field the instrument with a fixed PHA-detector distance (i.e., $\sim 27$ cm) as close as possible to the object (i.e., object-PHA distance $\sim 3$ cm) and use the x-ray framing camera available at OMEGA. This leaves us only two options for increasing the signal levels on the detector: 1) increasing the object solid angle to the pinhole by increasing the pinhole size [FIG. 1(a)] or 2) increasing object radiation power by increasing the Ar tracer amount. One must consider the trade-off due to these options. For example, as pinhole size is increased, the spatial resolution deteriorates because the signals observed at every point on the detector are integrated over a larger area on the source as illustrated in FIG. 1(b). When Ar fraction is increased, one has to consider its effects on the implosion hydrodynamics[13]. The pinhole size needs to be optimized taking into account these details.

Pinholes are arranged in a hexagonal pattern because this allows the object images to fill the detector plane most efficiently. Pinhole separation, $l$, is optimized based on the target image size, $FM$, where $F$ is the object size and $M$ is the magnification [FIG. 1(c)]. The distance between adjacent image centers is $l(M+1)$, which defines the maximum image size allowed for given $l$ and $M$. If the image size is larger than $l\,(M+1)$, the images start

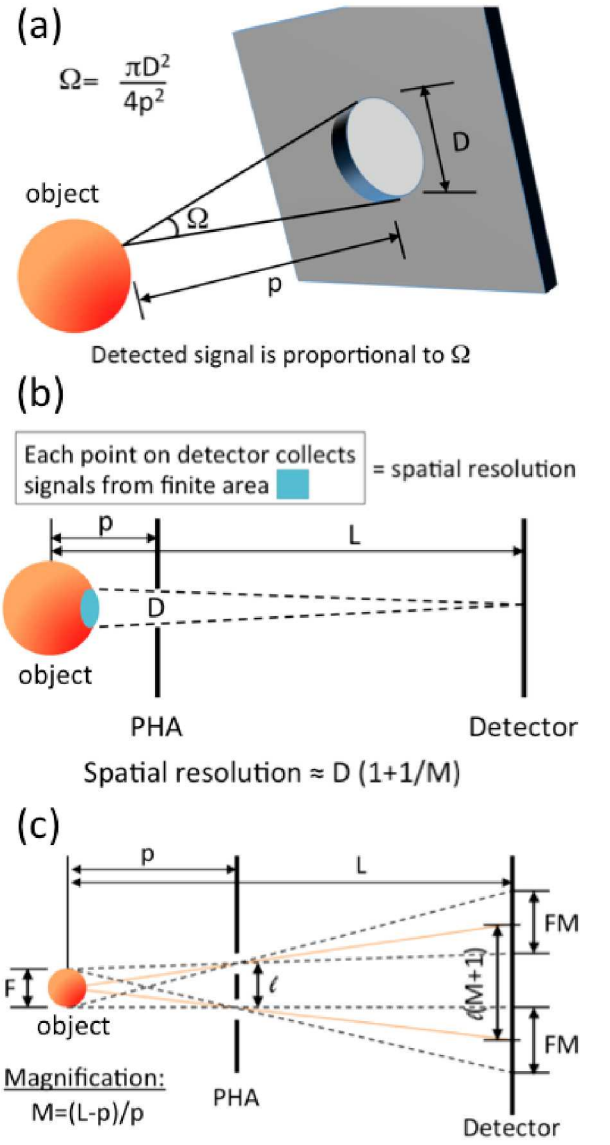


FIG. 1. (a) The signal collected through a pinhole is proportional to the source-to-pinhole solid angle, (b) spatial resolution is determined by object-pinhole-detector distances, (c) magnification is determined by object-pinhole distance, $p$, and object-detector distance, $L$. Optimal pinhole separation, $l$, is determined so that images of size $FM$ do not overlap.

to overlap, which complicates the interpretation. Thus, $l$ is determined such that $FM \lesssim l\,(M+1)$.

Once the maximum allowed image size is determined, appropriate tilt is determined based on MCP strip width, $K$, so that the detector samples object spatial information most efficiently at each photon energy. In other words, the images aligned vertically across the MCP width should have a gradual horizontal shift so that, for every photon energy, they provide spatial information of a slightly different point in object space. The ideal tilt is

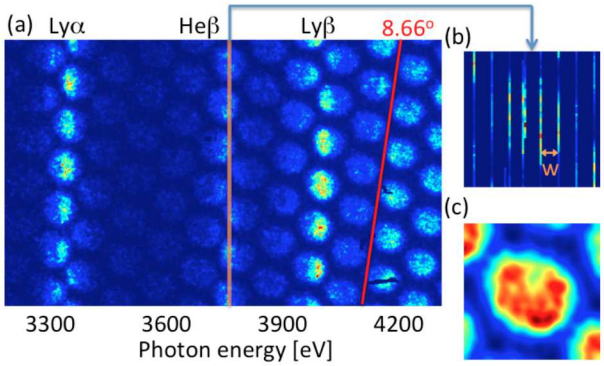


FIG. 2. (a) MMI data with an appropriate pinhole array tilt, (b) monochromatic image reconstructed from a single pixel-column at He-$\beta$ line center, (c) narrow-band He-$\beta$ image reconstructed over its line width (i.e., $\sim$ 60eV).

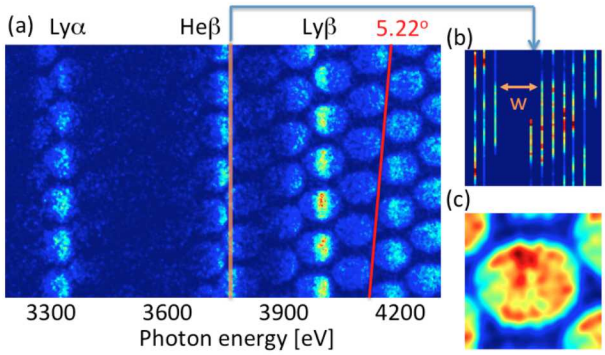


FIG. 3. (a) MMI data with an inappropriate pinhole array tilt, (b) monochromatic image reconstructed from a single pixel-column at He-$\beta$ line center, (c) narrow-band He-$\beta$ image reconstructed over its line width (i.e., $\sim$ 60eV).

computed by:

$$\theta = \arctan\left(\frac{\sqrt{4/3}l\,(M+1)}{K}\right) \quad (1)$$

as discussed in Ref.[6].

An example of MMI data with an appropriate PHA tilt is shown in FIG. 2(a). Hexagonally arranged implosion core images are shown with horizontal spectral axis. Due to K-shell line emission from Ar in the implosion core, images appearing around the photon energies associated with Ar Ly-$\alpha$ ($\sim$3320 eV), He-$\beta$ ($\sim$3686 eV), and Ly-$\beta$ ($\sim$3935 eV) are brighter. The designed tilt angle based on Eq. (1) was 8.95°, and the data show $(8.66 \pm 0.10)^\circ$. As designed, this image array efficiently provides spatial information at each photon energy. For example, FIG. 2(b) shows an image reconstructed from one-pixel column of the MMI data at He-$\beta$ line center (i.e., orange line) . Each pixel along this column is re-located into a single, common image plane based on the position relative to their nearest image centers[9]. This single column provides strips of object spatial information, which are uniformly separated over the image plane.

An example of MMI data with an inappropriate PHA tilt is shown in FIG. 3(a). While we used the same pinhole array design, it was misaligned in the MMI nose tip, which resulted in a significantly different tilt angle, $(5.22 \pm 0.02)^\circ$, in the data. The one pixel-column image provides strips, which are not uniformly distributed across the image, and thus, the spatial sampling is biased [FIG. 2(b)].

For both cases, one pixel-column does not reconstruct the whole image and adjacent pixel-columns are needed, which are at slightly different photon energies. Thus, the largest strip separation in the one pixel-column image, $w$, defines the minimum width required to reconstruct the whole image, which we call the reconstruction width or sampling width. On one hand, the appropriate case shown in FIG. 2 has $w = 8$ pixels. Thus, 8 pixel-columns are needed to fully reconstruct the image, which correspond to 15 eV for this particular data set based on the extracted spectral axis[9]. Thus, the whole image can be reconstructed with a much narrower width than the spectral line width, where its FWHM is approximately 60 eV. By extending the narrow-band width to its FWHM, one can improve the signal-to-noise ratio (S/N) and form a reliable He-$\beta$ line image [FIG. 2(c)]. On the other hand, the inappropriate case shown in FIG. 5 has $w = 20$ pixels, which corresponds to 44 eV. This is still narrower than the FWHM of the He-$\beta$ line. However, this means that the last pixel-column added to form the whole image comes from $44/2 = 22$ eV away from the line center. The overall intensity from this pixel-column is systematically lower than that of the line-center, and the spatial information at the center of the gap, $w$, has to rely significantly on the intensity correction discussed in Eq. (3) and (4) of Ref.[9]. Also, even after reconstructing the full image, the S/N of the large gap region is still very low. Accordingly, the reconstructed image structure becomes less reliable around the large gap region.

To summarize, the pinhole array needs to be tilted at an appropriate angle to achieve efficient spatial sampling and minimize the reconstruction width, $w$. Reliable MMI diagnostics further require that the spectral width corresponding to $w$ is much narrower than the FWHM of the diagnostic lines such as He-$\beta$ and Ly-$\beta$. Those line widths need to be estimated from conditions predicted with hydrodynamic simulations and taken into account to optimize the PHA design.

The extracted one pixel-column image such as FIG. 2(b) and FIG. 3(b) gives some idea on how reliable the recorded MMI data are. However, they do not directly answer how critical it is to satisfy this criterion. To better illustrate this point, we perform a synthetic investigation in Sec. IV using the spectral model discussed in Sec. III.

## III. SPECTRAL MODEL

The spectral model used in this article computes emergent spectra at every point on the image plane, $I_\nu\,(x,\,y)$, and then $I_\nu\,(x,\,y)$ is used to compute both synthetic MMI data and expected images. The case of investigation is an OMEGA direct-drive Ar-doped $D_2$-filled ICF implosion because it has been one of our main applications of the MMI diagnostics[10–12]. The ICF implosion core is the object for the synthetic data, and we define it as a sphere of uniform $T_e$ and $n_e$ to simplify the interpretation of the synthetic investigation. The capsule is initially filled with 20 atm of $D_2$ with 0.18% atomic concentration of Ar. Ar photon-energy dependent emissivity and opacity are computed for given $T_e$ and $n_e$, and emergent spectra are computed by solving radiation transport along each chord parallel to the line-of-sight[12].

To compute the Ar emissivity, $\epsilon_\nu$, and opacity, $\kappa_\nu$, necessary atomic data are computed by Flexible Atomic Code (FAC)[14], and Ar level populations are solved for the given $T_e$ and $n_e$ with a collisional-radiative model, ABAKO[15]. We used the Stewart and Pyatt model[16] for continuum lowering effects and the escape factor approximation to account for radiation transport effects on the populations[17]. Spectral emissivity and opacity are computed from the calculated populations including detailed Stark line profiles computed by MERL[18].

Emergent spectra are computed along each chord on the image plane by numerically integrating radiation transport equation assuming parallel ray tracing[19]:

$$I_\nu\,(x,\,y) = \int_{z_{rear}}^{z_{front}} \frac{\epsilon_\nu\,(x,\,y,\,z)}{\kappa_\nu\,(x,\,y,\,z)} \left\{1 - e^{-\tau_\nu(x,\,y,\,z)}\right\} dz \tag{2}$$

$$\tau_\nu\,(x,\,y,\,z) = \int_{z}^{z_{front}} \kappa_\nu\,(x,\,y,\,z')\,dz' \tag{3}$$

where the $z$ axis is parallel to the line of sight, the $x$-$y$ plane is parallel to the image plane of the detector, $I_\nu(x,y)$ is the emergent intensity at $(x,y)$ on the source [erg/s/cm$^2$/sr/eV], $\tau_\nu$ is the optical depth from point $z$ in the object to the observer side of the object surface. The quantities $\epsilon_\nu\,(x,\,y,\,z)$ and $\kappa_\nu\,(x,\,y,\,z)$ are determined with ABAKO at the given $T_e$ and $n_e$ if $(x,\,y,\,z)$ is inside the object and zero if it is outside the object.

Potential inaccuracy in the calculated emissivity and opacity does not affect the conclusions derived from the synthetic investigations performed in this article because $I_\nu(x,y)$ are used to calculate both synthetic MMI data and expected images. What we pursue is the discrepancies produced due to the discrete nature of MMI data and the details of data processing.

Expected narrow-band images are computed by integrating $I_\nu(x,y)$ over any given spectral range as:

$$I_{\Delta\nu}\,(x,\,y) = \int_{\Delta\nu} I_\nu\,(x,\,y)\,d\nu \tag{4}$$

where $\Delta\nu$ is the band-width of interest.

Synthetic MMI data are computed from the emergent spectra, $I_\nu(x,\,y)$, assuming parallel ray tracing. When MMI data are processed as discussed in Ref.[9], each MMI pixel, $(x_{mmi},\,y_{mmi})$, uniquely defines its photon energy $h\nu$ and its position on the image plane, $(x,\,y)$. Thus, using this pixel information provided from actual MMI data, one can compute each pixel of synthetic MMI data as $I_\nu(x,\,y)\Delta h\nu\Delta A$ by converting every pixel $(x_{mmi},\,y_{mmi})$ into $(x,\,y)$ and $h\nu$. $\Delta h\nu$ and $\Delta A$ are the finite spectral width and the finite area at the pixel $(x_{mmi},\,y_{mmi})$.

One concern is the validity of parallel ray tracing for the synthetic MMI data modeling. While photons going through pinholes are not precisely parallel, the parallel ray assumption is still valid for our applications. Based on the object size of 100 $\mu$m and object-PHA distance of 3 cm, rays through a single pinhole deviate from parallel by less than $\theta < \arctan(100\,\mu\text{m}/3\,\text{cm}) = 0.2°$. This maximum deviation in angle can be interpreted in terms of the maximum deviation on the image plane as (100 $\mu$m)$\times \sin(0.2) < 0.3\,\mu$m, which is much smaller than the typical spatial resolution of the image, $\Delta x \approx 11\mu$m.

Photons through different pinholes have a larger deviation from the parallel rays. On typical data, pinholes used to project images on a single MCP are separated by a maximum of $\sim$ 2 mm. Then, photons going through those pinholes could deviate from parallel up to $\theta < \arctan(2\,\text{mm}/3\,\text{cm}) = 3.8°$. Along the maximum chord length in the object, this results in a chord deviation of (100 $\mu$m)$\times \sin(3.8°) = 6.6\,\mu$m on the image plane. This deviation is still less than the spatial resolution of the instrument. Furthermore, this deviation is an upper bound because usually only a smaller portion of the MMI data are used in the analysis. For example, for He-$\beta$ and Ly-$\beta$ analysis, the most distant pinholes used in the analysis are separated by less than 1 mm, and thus its deviation on the image plane is less than 3.3 $\mu$m. Hence, parallel ray tracing is a good approximation to interpret the photon paths through the object for many MMI applications including ours.

## IV. IMPACT OF CRITERION ON MMI SPATIAL SAMPLING

The quality of the MMI data depends on whether or not $w$ is significantly narrower than the spectral line width. In this section, we synthetically investigate the impact of the criterion on the reliability of the extracted spatial information. This can be demonstrated by reconstructing images from the synthetic MMI data that do and do not satisfy the criterion and comparing them with the expected images.

First, MMI data with an appropriate pinhole array are created using a uniform sphere of 100 $\mu$m diameter, $T_e$=1500, and $n_e$=1.5 $\times$ 10$^{24}$ cm$^{-3}$. The PHA pattern and the photon energy axis are those from the appropriate data shown in FIG. 2(a). The conditions are the

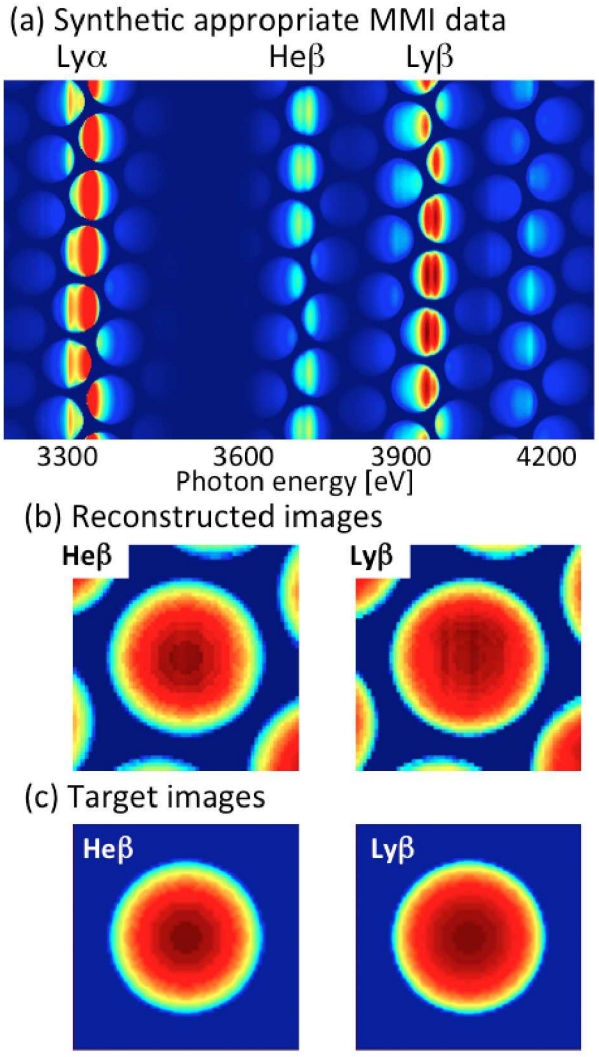


FIG. 4. (a) Synthetic MMI data with an appropriate PHA tilt and with the minimum reconstruction width, $w$, much narrower than the spectral line width, (b) Ar He-$\beta$ and Ly-$\beta$ images reconstructed from the synthetic MMI data, (c) expected Ar He-$\beta$ and Ly-$\beta$ images

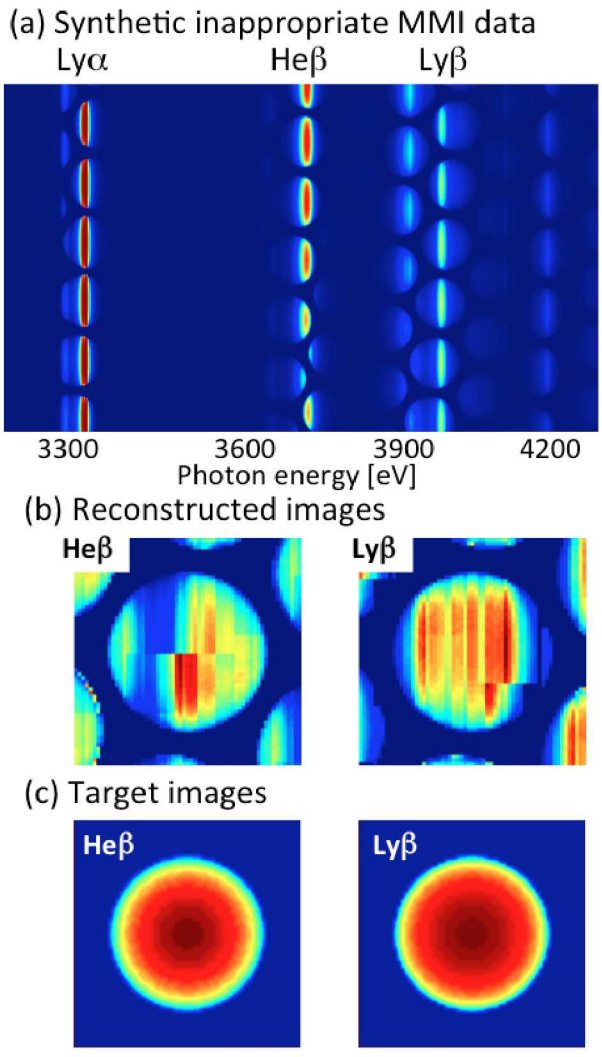


FIG. 5. (a) Synthetic MMI data with an inappropriate PHA tilt and with the minimum reconstruction width, $w$, broader than the spectral line width, (b) Ar He-$\beta$ and Ly-$\beta$ images reconstructed from the synthetic MMI data, (c) expected Ar He-$\beta$ and Ly-$\beta$ images

values representative of FIG. 2(a) based on the analysis of its space-integrated spectra. Thus, as already discussed in Sec. II, $w = 8$ pixels (i.e., ∼15 eV) and the FWHM of the He-$\beta$ and Ly-$\beta$ lines are roughly 60 eV, which satisfies $w \ll$FWHM.

FIG. 4(a) shows the resultant synthetic MMI data. Because $w$ is much narrower than the FWHM of the spectral lines, the reconstructed He-$\beta$ and Ly-$\beta$ images shown in FIG. 4(b) agree very well with the expected target images shown in FIG. 4(c).

Next, inappropriate MMI data are synthetically created using a uniform sphere of 100 $\mu$m diameter, $T_e$=1000 eV, and $n_e$=3 × $10^{23}$ cm$^{-3}$. The PHA pattern and the photon energy axis are those from the actual inappropriate MMI data shown in FIG. 3(a). Thus, the minimum width required to reconstruct image is $w$=20 pixels (i.e., 44 eV) as discussed in Sec. II. One reason why 3(c) still shows a reasonable image is that $w$ is still narrower than the line width (∼ 60 eV) while it is not significantly narrower. Thus, to show an extreme case, $n_e$ is purposely lowered so that $w$ becomes even broader than its Stark line width (∼16-19 eV).

FIG. 5(a) is the resultant synthetic MMI data, which show much narrower spectral features compared to FIG. 3(a). FIG. 5(b) shows the reconstructed Ar He-$\beta$ and Ly-$\beta$ images. Compared to the expected images [FIG. 5(c)], the reconstructed images have a lot of artificial structure originating from the discrete nature of the MMI data, which is amplified due to $w >$ FWHM.

## V. CONCLUSIONS

The MMI instrument is an interesting diagnostic tool to study spatial structure of the ICF plasmas. This article discusses the criterion for reliable MMI diagnostics and its impact on the extracted spatial information. Reliable MMI data have the sampling width, $w$, much narrower than the FWHM of the spectral lines. Appropriate pinhole array tilt is critical to minimize $w$ for a given target image size and MCP strip width.

We synthetically demonstrated that MMI data with $w >$ FWHM produces significant bias in the sampled object spatial information. On one hand, the images reconstructed from appropriate MMI data are very similar to those of the expected images. On the other hand, the images from inappropriate MMI data show very different spatial structure from the expected ones. The artificial structure is always vertical due to the fact that the images are reconstructed by superposition of vertical strips originating from different pixel-columns. The presence of strong vertical structure on the image is likely a sign that the MMI data are flawed and is most likely due to not satisfying the criterion. Reliability in the conclusions derived from such inapropriate MMI data are limited.

## ACKNOWLEDGEMENT

This work was supported by DOE/NLUF Grant Nos. DE-NA0000859 and DE-NA0002267, and LLNL.

[1] J. Nuckolls, L. Wood, A. Thiessen, and G. Zimmerman, Nature **239**, 139 (1972).
[2] J. D. Lindl, P. Amendt, R. L. Berger, S. G. Glendinning, S. H. Glenzer, S. W. Haan, R. L. Kauffman, O. L. Landen, and L. J. Suter, Physics of Plasmas **11**, 339 (2004).
[3] J. Lindl, O. Landen, J. Edwards, E. Moses, and N. Team, Physics of Plasmas (1994-present) **21**, 020501 (2014).
[4] D. S. Clark, M. M. Marinak, C. R. Weber, D. C. Eder, S. W. Haan, B. A. Hammel, D. E. Hinkel, O. S. Jones, J. L. Milovich, P. K. Patel, H. F. Robey, J. D. Salmonson, S. M. Sepke, and C. A. Thomas, Physics of Plasmas (1994-present) **22**, 022703 (2015).
[5] J. A. Koch, T. W. Barbee, N. Izumi, R. Tommasini, R. C. Mancini, L. A. Welser, and F. J. Marshall, Rev. Sci. Instrum. **76**, 073708 (2005).
[6] R. Tommasini, J. A. Koch, N. Izumi, L. A. Welser, R. C. Mancini, J. Delettrez, S. Regan, and V. Smalyuk, Rev. Sci. Instrum. **77**, 10E303 (2006).
[7] L. A. Welser, R. C. Mancini, J. A. Koch, S. Dalhed, R. W. Lee, I. E. Golovkin, F. Marshall, J. Delettrez, and L. Klein, Rev. Sci. Instrum. **74**, 1951 (2003).
[8] N. Izumi, T. W. Barbee, J. A. Koch, R. C. Mancini, and L. A. Welser, Rev. Sci. Instrum. **77**, 083504 (2006).
[9] T. Nagayama, R. C. Mancini, R. Florido, R. Tommasini, J. A. Koch, J. A. Delettrez, S. P. Regan, and V. A. Smalyuk, J Appl Phys **109**, 093303 (2011).
[10] T. Nagayama, R. C. Mancini, R. Florido, D. Mayes, R. Tommasini, J. A. Koch, J. A. Delettrez, S. P. Regan, and V. A. Smalyuk, Physics of Plasmas (1994-present) **21**, 050702 (2014).
[11] T. Nagayama, R. C. Mancini, R. Florido, R. Tommasini, J. A. Koch, J. A. Delettrez, S. P. Regan, V. A. Smalyuk, L. A. Welser-Sherrill, and I. E. Golovkin, Rev. Sci. Instrum. **79**, 10E921 (2008).
[12] T. Nagayama, R. C. Mancini, R. Florido, D. Mayes, R. Tommasini, J. A. Koch, J. A. Delettrez, S. P. Regan, and V. A. Smalyuk, Physics of Plasmas **19**, 082705 (2012).
[13] J. MacFarlane, I. Golovkin, R. Mancini, L. Welser, J. Bailey, J. Koch, T. Mehlhorn, G. Rochau, P. Wang, and P. Woodruff, Phys. Rev. E **72**, 066403 (2005).
[14] M. F. Gu, Can. J. Phys. **86**, 675 (2008).
[15] R. Florido, R. Rodríguez, J. M. Gil, J. G. Rubiano, P. Martel, E. Mínguez, and R. C. Mancini, Phys. Rev. E **80**, 56402 (2009).
[16] J. C. Stewart and K. D. J. Pyatt, The astrophysical Journal **144**, 1203 (1966).
[17] R. C. Mancini, R. F. Joyce, and C. F. Hooper, Jr., J. Phys. B: At. Mol. Phys. **20**, 2975 (1987).
[18] R. C. Mancini, D. P. Kilcrease, L. A. Woltz, and C. F. Hooper, Jr., Computer Physics Communications **63**, 314 (1991).
[19] D. Mihalas, *Stellar Atmospheres*, Astronomy and Astrophysics Series (W. H. Freeman, 1978).